# The $^{14}N(^{7}Be,^{8}B)^{13}C$ reaction and the $^{7}Be(p,\gamma)^{8}B$ $S$ factor

A. Azhari,[1] V. Burjan,[2] F. Carstoiu,[3] C. A. Gagliardi,[1] V. Kroha,[2] A. M. Mukhamedzhanov,[1] X. Tang,[1] L. Trache,[1] and R. E. Tribble[1]

[1]*Cyclotron Institute, Texas A&M University, College Station, Texas 77843*

[2]*Institute for Nuclear Physics, Czech Academy of Sciences, Prague-Řež, Czech Republic*

[3]*Institute of Physics and Nuclear Engineering, Bucharest, Romania*

(Received 20 July 1999; published 8 October 1999)

The $^{14}N(^{7}Be,^{8}B)^{13}C$ reaction was studied using an 85 MeV $^{7}Be$ radioactive beam. The asymptotic normalization coefficients for the virtual transitions $^{7}Be+p\leftrightarrow{}^{8}B$ were determined from the measured cross section. These coefficients specify the amplitude of the tail of the $^{8}B$ overlap function in the $^{7}Be+p$ channel, and were used to calculate the astrophysical $S$ factor for the direct capture reaction $^{7}Be(p,\gamma)^{8}B$ at solar energies $S_{17}(0)$. We find that $S_{17}(0)=16.6\pm1.9$ eV b.
[S0556-2813(99)01111-5]

PACS number(s): 25.60.Je, 26.65.+t, 26.20.+f, 25.60.Bx

New models of neutrino physics have emerged in light of the consistently lower than expected measured neutrino fluxes from the sun. $^{8}B$ neutrinos are central to this question. $^{8}B$'s produced in the $^{7}Be(p,\gamma)^{8}B$ reaction are the source of most or, in some cases, all solar neutrinos observed in several existing and planned solar neutrino experiments (e.g., Homestake, Kamiokande, Super-Kamiokande, SNO). Thus, the cross section or, equivalently, its astrophysical $S$ factor $S_{17}(0)$ plays a crucial role in providing better limits within neutrino models. There have been five direct measurements of this cross section using radioactive $^{7}Be$ targets with uncertainties less than 20%. When the measured $S$ factors are extrapolated from the observed energy ranges down to $E_{\text{c.m.}}=0$, each experiment provides a determination of $S_{17}(0)$ to $\approx10\%$, but two of these results [1,2] are near 25 eV b, while the other three [3–5] are near 18 eV b. All of these experiments are consistent with the predicted energy dependence of $S(E)$ [6–9], indicating this discrepancy is due to unresolved problems in absolute normalizations. Therefore, the most recent review of solar fusion rates adopted a value $S_{17}(0)=19^{+4}_{-2}$ eV b [10], making $S_{17}(0)$ the most uncertain input for solar model calculations and a high priority for new measurements. This review also emphasized the importance of additional indirect determinations of $S_{17}(0)$ that are sensitive to different systematic effects from those present in the direct cross section measurements. One indirect determination, based on Coulomb dissociation of $^{8}B$ [11,12], favors the lower values of $S_{17}(0)$. But the reliability of Coulomb dissociation to determine astrophysical $S$ factors at stellar energies has not yet been verified [10].

At solar energies direct capture processes proceed through the tail of the nuclear overlap function [6]. This is especially applicable to the $^{7}Be(p,\gamma)^{8}B$ reaction, given the very weakly bound proton in $^{8}B$. At distances larger than the nuclear radius, the shape of this tail is determined by the Coulomb interaction, so the capture rate can be calculated accurately if one knows the amplitude of the tail. The asymptotic normalization coefficients (ANC) for $^{7}Be+p\leftrightarrow{}^{8}B$ specify the amplitude of the tail of the $^{8}B$ overlap function in the two-body channel when the $^{7}Be$ core and the proton are separated by a distance large compared to the nuclear radius. At these distances the overlap function is equal to a normalized Whittaker function, where the normalization factor is the ANC. The ANC can be determined from measurements of nuclear reactions, such as peripheral nucleon transfer, where cross sections are orders of magnitude larger than the direct capture reactions themselves. Therefore, it provides a convenient approach to determine direct capture $S$ factors at zero energy. In a previous study [13], we tested this technique by comparing measured $S$ factors for $^{16}O(p,\gamma)^{17}F$ with calculations based on ANC's measured in the peripheral proton transfer reaction $^{16}O(^{3}He,d)^{17}F$ and found the agreement was better than 9%.

An earlier experiment attempted to measure the ANC's for $^{7}Be+p\leftrightarrow{}^{8}B$ with the reaction $^{2}H(^{7}Be,^{8}B)n$ [14]; however, interpretation of that experiment was complicated by uncertainties in the choice of optical model parameters [15,16]. Recently, we reported an indirect determination of $S_{17}(0)=17.8\pm2.8$ eV b from a measurement of the ANC for $^{7}Be+p\leftrightarrow{}^{8}B$ in the $^{10}B(^{7}Be,^{8}B)^{9}Be$ reaction [17]. Here, we report a second indirect measurement of this capture rate at solar energies via a determination of the asymptotic normalization coefficients for $^{7}Be+p\leftrightarrow{}^{8}B$ from the $^{14}N(^{7}Be,^{8}B)^{13}C$ reaction. This experiment was motivated by more than a need to verify the results obtained from the $^{10}B(^{7}Be,^{8}B)^{9}Be$ reaction using a different system. Improvements in experimental hardware, beam quality, and target uniformity allowed for a measurement with lower experimental uncertainties.

The $^{7}Be$ radioactive beam was produced via the reaction $^{1}H(^{7}Li,^{7}Be)n$, using $\approx150$ enA of 135 MeV $^{7}Li$ beam from the Texas A&M University K500 superconducting cyclotron irradiating a 2.8 mg/cm$^2$ thick $LN_2$-cooled cryogenic $H_2$ gas cell with 42 mg/cm$^2$ Havar windows. A 69 mg/cm$^2$ aluminum degrader reduced the $^{7}Li$ beam energy before entering the gas cell. 85 MeV $^{7}Be$ recoils entered the Texas A&M Momentum Achromat Recoil Spectrometer (MARS) [18,19] at 0°, where they were separated from the primary beam and

 ©1999 The American Physical Society

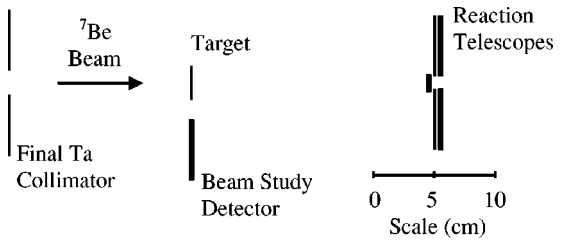


FIG. 1. Target and detector configuration.

other reaction products. Slits distributed throughout MARS were employed to optimize the $^7$Be beam size and energy and angular spread. The detectors shown in Fig. 1 were located at the MARS focal plane.

For beam studies a $5\times5$ cm$^2$, 1000-$\mu$m thick, two-dimensional position-sensitive Si strip detector was mounted on the target ladder. This detector consisted of 16 resistive strips on one side allowing for both vertical and horizontal position measurements. The back of this detector consisted of a solid piece which provided the total energy of the particles. Due to the small size of the beam spot, only the eight central strips were included in the electronics. The beam spot dimensions were measured to be 2.5 mm horizontal by 3.6 mm vertical, both full-width at half maximum (FWHM). This detector was also used to calibrate the $^7$Be yield relative to the measured $^7$Li beam current at the MARS Faraday cup. Momentum slits, positioned near the Faraday cup, were used to set the energy spread of the beam at 1.6 MeV (FWHM). A set of horizontal and vertical slits placed 74 cm in front of the target were used to determine the angular spread of the beam by closing the slits to $5\times5$ mm$^2$ and scanning the beam profile in the horizontal and vertical directions. Beam intensity was found to be uniform across the scanned region. The angular spread was measured to be 1.8° horizontal by 0.6° vertical (full widths). Better than 99.5% purity for the $^7$Be radioactive beam was obtained at the secondary target, with only lower energy $\alpha$ particles as contaminants. The $^7$Be intensity on target was checked frequently and was typically $\sim$80 kHz. This represents an increase of over 30% in beam intensity, while simultaneously reducing the horizontal emittance by 63% and the vertical emittance by 78% from the previous $^{10}$B($^7$Be,$^8$B)$^9$Be study [17].

The reaction target consisted of 1.50 mg/cm$^2$ melamine ($C_3N_6H_6$) on 20 $\mu$g/cm$^2$ C and 20 $\mu$g/cm$^2$ collodion backings. Target properties such as thickness and uniformity were verified directly by the $^7$Be beam. The reaction detector assemblies described below were used to compare the energy of the beam through a blank target holder and through the target foil. The $dE/dx$ measurement was compared to results from the computer code SRIM [20] to confirm the thickness of the target. A Monte Carlo simulation was used to analyze the target in and target out data. The energy shift, due to average target thickness, was reproduced along with the broadening of the $^7$Be beam energy spectrum due to nonuniformities and straggling. The average thickness was verified to be $1.50\pm0.05$ mg/cm$^2$, where the uncertainty is mainly due to the calculation of the straggling using the code SRIM. Also, the uniformity over the area of the $^7$Be beam was found to be better than 7%, which has no significant effect on the results. This represents a significant improvement in uniformity from the previous measurement and is critical in obtaining better energy resolution.

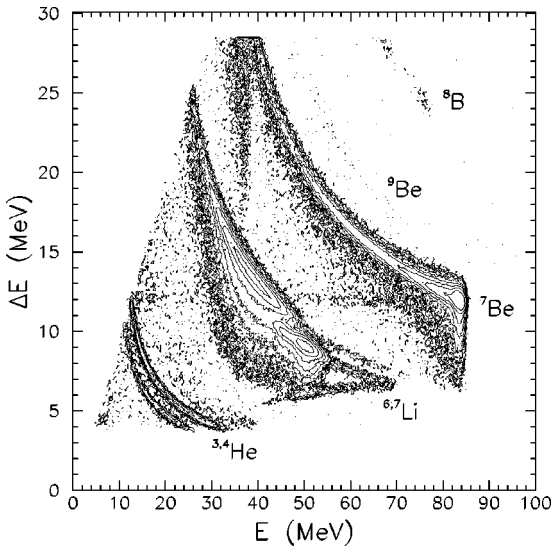


FIG. 2. Particle identification plot of energy loss versus total energy.

Both $^7$Be elastic scattering and $^8$B produced in the reaction $^{14}$N($^7$Be,$^8$B)$^{13}$C were observed simultaneously by the reaction telescopes shown in Fig. 1. The telescopes consisted of $5\times5$ cm$^2$, 105-$\mu$m thick Si $\Delta E$ detectors, backed by 1000-$\mu$m thick Si $E$ detectors. The $\Delta E$ detectors included read-outs from 16 separate resistive strips to provide two-dimensional position information for each event, together with an independent read-out of the energy loss. The detector geometry was optimized for maximum geometric efficiency while minimizing physical damage from the $^7$Be beam. Particle identification was achieved from the $\Delta E-E_{\text{total}}$ information, as shown in Fig. 2.

$^7$Be elastic scattering data were used to optimize simulation parameters and to validate both our understanding of the beam and detector properties and our choice of optical model parameters. A detailed Monte Carlo simulation of the experiment included all the measured properties of the beam, energy loss and straggling in the target, the reaction kinematics, and the finite resolution of the detectors. Detector solid angles were simulated as a function of scattering angle, including the overall energy and angular resolutions. Elastic scattering yields were obtained from the data using $^7$Be events which were kinematically reconstructed by the analysis code based on the assumption that all events resulted from scattering off of $^{14}$N nuclei. Monte Carlo simulations were performed to predict the overall energy resolution of the elastic scattering $Q$-value spectrum integrated over scattering angle. Realistic angular distributions were used as inputs to simulate the elastic scattering of $^7$Be on each nuclear species in the melamine target. Figure 3 shows a fit of the kinematically reconstructed $Q$-value spectrum of the $^7$Be particles, together with individually simulated contributions from the N, C, and H. The shift in the $Q$ value of H and C to a lesser degree, from zero stems from using kinematic reconstruction appropriate for N as target nucleus. The sum of

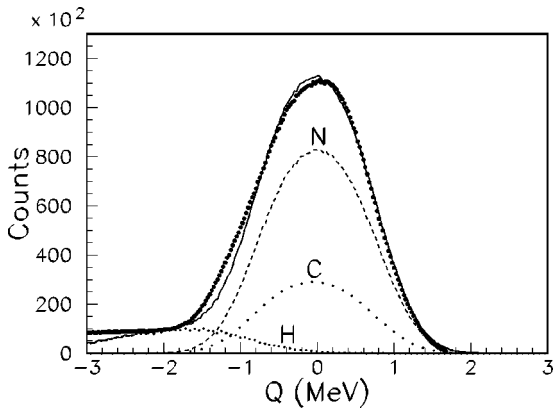


FIG. 3. $Q$-value spectrum of outgoing $^{7}$Be nuclei. The solid curve is a sum of contributions from Monte Carlo simulations of the elastic scattering of $^{7}$Be on $^{14}$N, $^{12}$C, and $^{1}$H, fitted over the region $-1.0$ MeV $< Q < 1.5$ MeV.

these contributions shows good agreement with the data, confirming our understanding of experimental resolutions. The tail extending to $Q < -2$ MeV is due to inelastic scattering of $^{7}$Be which was not included in the simulations. Figure 4 shows the resulting elastic scattering angular distribution using the solid angle factors obtained from the Monte Carlo simulation. In order to compare the measured angular distribution to optical model predictions, it was necessary to include the elastic scattering due to C and H in the target. Since finite resolution made it impossible to distinguish scattering from N and C, this was done by adding their contributions in the laboratory frame and then converting the results into a center-of-mass angular distribution using the kinematics appropriate for $^{7}$Be+$^{14}$N elastic scattering. Figure 4 shows this predicted angular distribution with and without a correction for finite angular resolution.

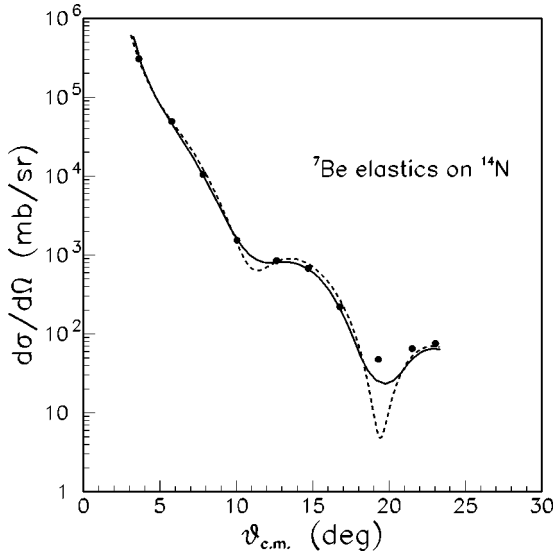


FIG. 4. Observed $^{7}$Be elastic scattering angular distribution. Statistical errors are smaller than the plotted data points. The overall normalization uncertainty is $\pm 5.0\%$. The dashed curve is the predicted angular distribution, summed over $^{14}$N, $^{12}$C, and $^{1}$H target nuclei, while the solid curve shows the same distribution corrected for finite angular resolution.

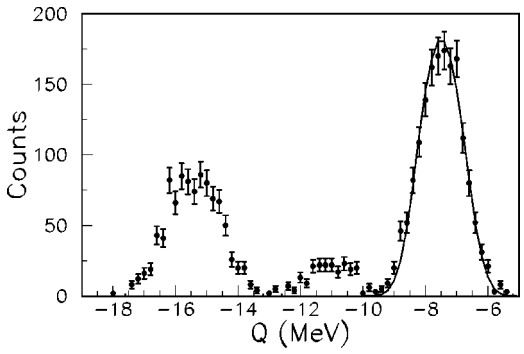


FIG. 5. $Q$-value spectrum of the outgoing $^{8}$B nuclei. The solid curve is the Monte Carlo simulation of the $^{14}$N($^{7}$Be,$^{8}$B)$^{13}$C(g.s.) reaction, normalized to the data over the region $-9.5$ MeV $< Q < -5.5$ MeV.

The elastic scattering angular distributions have been predicted using optical model parameters obtained from double folding model calculations convoluting Hartree-Fock density distributions with the effective interaction of Jeukenne, Lejeune, and Mahaux (JLM) [21]. The folded potentials have been renormalized to match the systematics observed in elastic scattering of $p$-shell nuclei at 9 to 16 MeV/nucleon—including $^{6}$Li+$^{12}$C [22], $^{7}$Li+$^{9}$Be, $^{7}$Li+$^{12}$C [23], $^{7}$Li +$^{13}$C, $^{10}$B+$^{9}$Be [24], $^{13}$C+$^{9}$Be, and $^{14}$N+$^{13}$C [25]. In total, eight angular distributions have been analyzed to obtain the renormalization factors needed to fit elastic scattering in this mass region. Since the JLM effective interactions are density and energy dependent, they provide a very good description of the mass dependence of the optical potential. Thus, the renormalization factors are nearly independent of the colliding system, minimizing the uncertainties due to the choice of optical parameters. Details regarding the optical potentials will be provided in a separate publication [26].

Figure 4 shows good agreement between the expected and observed elastic scattering angular distributions, especially since the calculations do not include contributions from inelastic scattering populating the $^{7}$Be first excited state, which is not resolved from the elastic scattering. High resolution elastic scattering studies in this energy region involving $^{7}$Li [26] projectiles imply that these excited states should contribute less than 15% of the total yield observed near the elastic scattering minima, and less than 1% at the maxima. It is important to recognize that Fig. 4 does not represent a fit to our measured data. Rather, it is a comparison between the measured absolute cross section for elastic scattering and the predicted absolute cross section from the folding model, with neither adjusted to match the other. The ratio of predicted cross section to data varies from unity by an average of only 3.0%, well within the 5% overall normalization uncertainty in our measured cross section.

Distorted-wave Born approximation (DWBA) calculations were used to predict the angular distribution for the reaction $^{14}$N($^{7}$Be,$^{8}$B)$^{13}$C. This cross section was then input to the Monte Carlo simulation using the same experimental parameters verified with the elastic $^{7}$Be's. Figure 5 shows

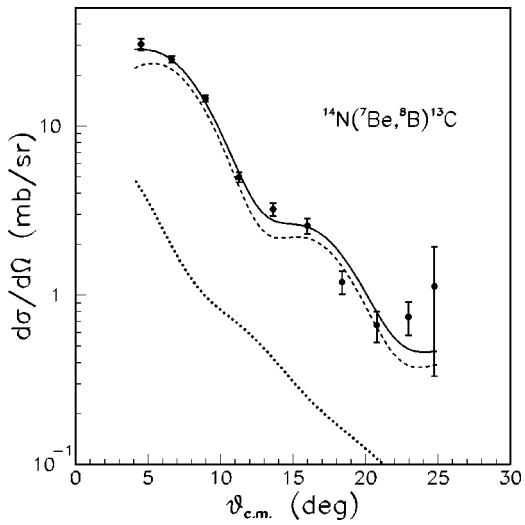


FIG. 6. Measured $^{14}$N($^{7}$Be,$^{8}$B)$^{13}$C angular distribution for those events in Fig. 5 that have $Q > -9.5$ MeV. The dashed and dotted curves show DWBA calculations of the dominant contributions from the $p_{1/2} \rightarrow p_{3/2}$ and $p_{1/2} \rightarrow p_{1/2}$ channels, respectively. The solid curve shows the total predicted angular distribution, normalized to the total cross section inferred from the *Q*-value fit in Fig. 5. All three curves have been corrected for finite angular resolution.

the *Q*-value spectrum for the outgoing $^{8}$B nuclei with a simulation of the transfer reaction. The $^{8}$B events around $-11$ and $-15$ MeV are due primarily to the $^{14}$N($^{7}$Be,$^{8}$B)$^{13}$C($3/2^{-}$, $E^{\star} = 3.68$ MeV) and $^{12}$C($^{7}$Be,$^{8}$B)$^{11}$B(g.s.) reactions, respectively. Figure 6 shows the measured $^{14}$N($^{7}$Be,$^{8}$B)$^{13}$C angular distribution for those outgoing $^{8}$B nuclei with $Q > -9.5$ MeV which correspond to ground state transfer events only.

For a peripheral transfer reaction, ANC's are extracted from the measured cross section by comparison to a DWBA calculation. In the $^{14}$N($^{7}$Be,$^{8}$B)$^{13}$C(g.s.) proton transfer reaction, the last proton in the ground state of $^{14}$N can be in the $p_{1/2}$ or $p_{3/2}$ orbitals and transfers to the $p_{1/2}$ or $p_{3/2}$ orbitals constituting the ground state of $^{8}$B. Thus, the experimental cross section is given by

$$\frac{d\sigma}{d\Omega} = C^2_{^8\mathrm{B},p_{3/2}} \left[ \frac{C^2_{^{14}\mathrm{N},p_{1/2}}}{b^2_{^{14}\mathrm{N},p_{1/2}}} \frac{\sigma_{p_{1/2}\rightarrow p_{3/2}}}{b^2_{^8\mathrm{B},p_{3/2}}} + \frac{C^2_{^{14}\mathrm{N},p_{3/2}}}{b^2_{^{14}\mathrm{N},p_{3/2}}} \frac{\sigma_{p_{3/2}\rightarrow p_{3/2}}}{b^2_{^8\mathrm{B},p_{3/2}}} \right] + C^2_{^8\mathrm{B},p_{1/2}} \left[ \frac{C^2_{^{14}\mathrm{N},p_{1/2}}}{b^2_{^{14}\mathrm{N},p_{1/2}}} \frac{\sigma_{p_{1/2}\rightarrow p_{1/2}}}{b^2_{^8\mathrm{B},p_{1/2}}} + \frac{C^2_{^{14}\mathrm{N},p_{3/2}}}{b^2_{^{14}\mathrm{N},p_{3/2}}} \frac{\sigma_{p_{3/2}\rightarrow p_{1/2}}}{b^2_{^8\mathrm{B},p_{1/2}}} \right], \quad (1)$$

where $\sigma$'s are the calculated DWBA cross sections for proton transfer from the $p_{3/2}$ and $p_{1/2}$ orbitals in $^{14}$N to the $p_{3/2}$ and $p_{1/2}$ orbitals in $^{8}$B, $b$'s are the asymptotic normalization constants for the single-particle orbitals used in the DWBA calculation, $C_{^{14}\mathrm{N}}$'s are the ANC's for $^{14}\mathrm{N} \leftrightarrow {}^{13}\mathrm{C} + p$, and $C_{^8\mathrm{B},p_{3/2}}$and $C_{^8\mathrm{B},p_{1/2}}$are the ANC's for $^{7}\mathrm{Be} + p \leftrightarrow {}^{8}\mathrm{B}$. The values for the $^{14}$N ANC's were previously determined to be $C^2_{^{14}\mathrm{N},p_{1/2}} = 18.6(12)$ fm$^{-1}$ and $C^2_{^{14}\mathrm{N},p_{3/2}} = 0.93(14)$ fm$^{-1}$ from a study of the $^{13}$C($^{14}$N,$^{13}$C)$^{14}$N reaction [25].

DWBA calculations were carried out with the finite-range code PTOLEMY [27], using the full transition operator. The $^{7}\mathrm{Be} + {}^{14}\mathrm{N}$ distorted waves were calculated with the same folding model optical potential used in the elastic scattering calculations above, while the $^{8}\mathrm{B} + {}^{13}\mathrm{C}$ optical potential was derived from a similar folding model calculation. The peripheral nature of the reaction was verified by comparing the results of DWBA calculations while varying the parameters of the single-particle Woods-Saxon potential wells over the ranges $r_0 = 1.0 - 1.3$ fm and $a = 0.5 - 0.7$ fm. The predicted cross section integrated over $6° < \theta_{\mathrm{c.m.}} < 25°$ changed by 40%, while the inferred ANC's only changed by $\pm 3.2\%$. Figure 6 shows the data for the transfer reaction and the DWBA prediction. All four contributions to the total cross section in Eq. (1) were included in the solid line, although only the $p_{1/2} \rightarrow p_{3/2}$ and $p_{1/2} \rightarrow p_{1/2}$ contributions are shown. The $p_{3/2} \rightarrow p_{3/2}$ and $p_{3/2} \rightarrow p_{1/2}$ components are not shown in the figure since, together, they contribute about five times less than the $p_{1/2} \rightarrow p_{1/2}$ component. As evident in Fig. 6, the angular resolution of the present experiment is insufficient to distinguish the small difference between the angular distributions for the different transitions over the angular region studied. Therefore, we calculated the $^{14}$N($^{7}$Be,$^{8}$B)$^{13}$C(g.s.) angular distribution using $C^2_{^8\mathrm{B},p_{1/2}} / C^2_{^8\mathrm{B},p_{3/2}} = 0.157$, as determined from microscopic calculations [28]. Figure 6 shows that our observed angular distribution is in very good agreement with the predicted shape, normalized to the cross section that we found from the *Q*-value fit described below.

To determine the $^{8}$B ANC's, we have fit the angle-integrated *Q*-value spectrum shown in Fig. 5 to obtain the total $^{14}$N($^{7}$Be,$^{8}$B)$^{13}$C(g.s.) cross section. The predicted angular distribution of Fig. 6 was input to the Monte Carlo simulation—which calculated the shape, location, and magnitude of the ($^{7}$Be,$^{8}$B) *Q*-value peak. $\chi^2$ minimization provided the best fit to the measured *Q*-value spectrum over the range $-9.5$ MeV $< Q < -5.5$ MeV and determined the absolute cross section for populating the $^{9}$Be ground state to be $\sigma = 1.131 \pm 0.066$ mb. This gives $C^2_{p_{3/2}} = 0.371 \pm 0.043$ fm$^{-1}$ for $^{8}\mathrm{B} \rightarrow {}^{7}\mathrm{Be} + p$. A detailed analysis of uncertainties and their sources was performed. The contributions to the uncertainties are: statistics (2.6%), absolute normalization of the measured cross section (5.0%), inputs to the Monte Carlo simulation (1.4%), inputs to the DWBA (8.1%), and knowledge of the $^{14}$N ANC (6.4%). These values are consistently lower than those reported for the $^{10}$B($^{7}$Be,$^{8}$B)$^{9}$Be reaction [17], especially the uncertainties from simulation and the ANC of the second vertex. Therefore the total uncertainty in the $^{8}$B ANC was reduced from 16% to 12%. However, the major contribution to the uncertainty arising from the DWBA calculations continues to be the limiting parameter in these determinations.

The relation between the $^{8}$B ANC's and $S_{17}(0)$, which was derived in [6], is

$$S_{17}(0) = \frac{38.6\ \text{eV b}}{\text{fm}^{-1}} (C^2_{^8\text{B},p_{3/2}} + C^2_{^8\text{B},p_{1/2}}). \qquad (2)$$

Thus, we conclude that $S_{17}(0) = 16.6 \pm 1.9$ eV b for $^{7}\text{Be}(p,\gamma)^{8}\text{B}$. This is in very good agreement with the results obtained from our previous ANC measurement [17] and the three smaller direct measurements of the $^{7}\text{Be}(p,\gamma)^{8}\text{B}$ cross section [3–5] and is more than $3\sigma$ below the two larger direct measurements [1,2]. This result provides strong, independent confirmation of the procedure in Ref. [5], which chose to disregard the two larger measurements and calculate $S_{17}(0)$ based on a weighted mean of the three smaller direct measurements alone.

We are currently studying the degree of correlation between the uncertainties calculated for $S_{17}(0)$ in the present work and in Ref. [17]. This correlation arises solely from the methods used to obtain the optical model potentials. After resolving this issue, the two experimental results can be combined to determine a final value for $S_{17}$ with smaller uncertainty using the ANC technique.

This work was supported in part by the U.S. Department of Energy under Grant No. DE-FG03-93ER40773 and by the Robert A. Welch Foundation.

[1] P. D. Parker, Phys. Rev. **150**, 851 (1966).
[2] R. W. Kavanagh, T. A. Tombrello, J. M. Mosher, and D. R. Goosman, Bull. Am. Phys. Soc. **14**, 1209 (1969).
[3] F. J. Vaughn, R. A. Chalmers, D. Kohler, and L. F. Chase, Phys. Rev. C **2**, 1657 (1970).
[4] B. W. Filippone, A. J. Elwyn, C. N. Davids, and D. D. Koetke, Phys. Rev. Lett. **50**, 412 (1983); Phys. Rev. C **28**, 2222 (1983).
[5] F. Hammache *et al.*, Phys. Rev. Lett. **80**, 928 (1998).
[6] H. M. Xu, C. A. Gagliardi, R. E. Tribble, A. M. Mukhamedzhanov, and N. K. Timofeyuk, Phys. Rev. Lett. **73**, 2027 (1994).
[7] P. Descouvemont and D. Baye, Nucl. Phys. **A567**, 341 (1994).
[8] A. Csoto, Phys. Lett. B **394**, 247 (1997).
[9] P. Descouvemont and D. Baye, Phys. Rev. C **60**, 015803 (1999).
[10] E. G. Adelberger *et al.*, Rev. Mod. Phys. **70**, 1265 (1998).
[11] T. Motobayashi *et al.*, Phys. Rev. Lett. **73**, 2680 (1994).
[12] T. Kikuchi *et al.*, Eur. Phys. J. A **3**, 213 (1998).
[13] C. A. Gagliardi *et al.*, Phys. Rev. C **59**, 1149 (1999).
[14] W. Liu *et al.*, Phys. Rev. Lett. **77**, 611 (1996).
[15] C. A. Gagliardi, A. M. Mukhamedzhanov, R. E. Tribble, and H. M. Xu, Phys. Rev. Lett. **80**, 421 (1998).
[16] J. C. Fernandes, R. Crespo, F. M. Nunes, and I. J. Thompson, Phys. Rev. C **59**, 2865 (1999).
[17] A. Azhari, V. Burjan, F. Carstoiu, H. Dejbakhsh, C. A. Gagliardi, V. Kroha, A. M. Mukhamedzhanov, L. Trache, and R. E. Tribble, Phys. Rev. Lett. **82**, 3960 (1999).
[18] R. E. Tribble, R. H. Burch, and C. A. Gagliardi, Nucl. Instrum. Methods Phys. Res. A **285**, 441 (1989).
[19] R. E. Tribble, C. A. Gagliardi, and W. Liu, Nucl. Instrum. Methods Phys. Res. B **56/57**, 956 (1991).
[20] J. F. Ziegler, J. P. Biersack, and U. Littmark, *The Stopping and Range of Ions in Solids* (Pergamon Press, New York, 1985), and accompanying computer code SRIM, version 96.xx.
[21] J. P. Jeukenne, A. Lejeune, and C. Mahaux, Phys. Rev. C **16**, 80 (1977).
[22] P. Schwandt *et al.*, Phys. Rev. C **24**, 1522 (1981).
[23] A. F. Zeller, Y.-W. Lui, R. E. Tribble, and D. M. Tanner, Phys. Rev. C **22**, 1534 (1980).
[24] A. M. Mukhamedzhanov *et al.*, Phys. Rev. C **56**, 1302 (1997).
[25] L. Trache, A. Azhari, H. L. Clark, C. A. Gagliardi, Y.-W. Lui, A. M. Mukhamedzhanov, R. E. Tribble, and F. Carstoiu, Phys. Rev. C **58**, 2715 (1998).
[26] L. Trache *et al.*, Phys. Rev. C (submitted).
[27] M. Rhoades-Brown, M. McFarlane, and S. Pieper, Phys. Rev. C **21**, 2417 (1980); **21**, 2436 (1980).
[28] A. M. Mukhamedzhanov and N. K.Timofeyuk, Sov. J. Nucl. Phys. **51**, 431 (1990).